Probing the Transition State-to-Intermediate Continuum: Mechanistic Distinction Between a Dry vs Wet Perepoxide in the Singlet Oxygen 'Ene' Reaction at the Air-Water Interface

Belaid Malek,¹ Wenchao Lu,^{2,3} Prabhu Prasad Mohapatra,^{1,3} Niluksha Walalawela,^{1,3} Shakeela Jabeen,^{1,3} Jianbo Liu,^{2,3*} and Alexander Greer^{1,3*}

¹ Department of Chemistry, Brooklyn College of the City University of New York, Brooklyn, New York 11210, United States

² Department of Chemistry and Biochemistry, Queens College of the City University of New York, 65-30 Kissena Blvd., Queens, New York, United States

³ Ph.D. Program in Chemistry, The Graduate Center of the City University of New York, 365 Fifth Avenue, New York, New York 10016, United States

Abstract

A mechanistic study is reported for the reactions of singlet oxygen (¹O₂) with alkene surfactants of tunable properties. Singlet oxygen was generated either top-down (photochemically) by delivery as a gas to an air-water interface or bottom-up (chemically) by transport to the air-water interface as a solvated species. In both cases, reactions were carried out in the presence of 7-carbon (7C), 9-carbon (9C), or 11-carbon (11C) prenylsurfactants [(CH₃)₂C=CH(CH₂)_nSO₃⁻ Na^+ (n = 4, 6, 8)]. Higher 'ene' hydroperoxide regioselectivities (secondary ROOH 2 to tertiary ROOH 3) were reached in delivering ¹O₂ top-down through-air as compared to bottom-up via aqueous solution. In the photochemical reaction, ratios of 2:3 increased from 2.5:1 for 7C, to 2.8:1 for 9C, and to 3.2:1 for 11C. In contrast, in the bubbling system that generated ¹O₂ chemically, the selectivity was all but lost, ranging only from 1.3:1 to 1:1. The phase-dependent regioselectivities appear to be correlated with the 'ene' reaction with photochemically generated, drier ¹O₂ at the air—water interface vs those with wetter ¹O₂ from the bubbling reactor. Density functional theorycalculated reaction potential energy surfaces (PESs) were used to help rationalize the reaction phase dependence. The reactions in the gas phase are mediated by perepoxide transition states with 32-41 kJ/mol binding energy for $C=C(\pi)$ ···¹O₂. The perepoxide species, however, evolve to welldefined stationary structures in the aqueous phase, with covalent C-O bonds and 85-88 kJ/mol binding energy. The combined experimental and computational evidence points to a unique mechanism for ¹O₂ 'ene' tunability in a perepoxide continuum from a transition state to intermediate.

Introduction

The singlet oxygen (${}^{1}O_{2}$) 'ene' reaction with formation of allylic hydroperoxides is an oxidation reaction of fundamental interest. Whether the ${}^{1}O_{2}$ 'ene' mechanism proceeds by a concerted or stepwise path has been a point of mechanistic interest and debate. A two-step nointermediate mechanism has been proposed suggesting a perepoxide transition state (TS). ${}^{1-3}$ A mechanism involving a perepoxide intermediate has also been proposed. ${}^{4-8}$ In this vein, we have pursued a unique experimental and theoretical approach to evaluate possible *borderline* mechanisms. Our reaction of ${}^{1}O_{2}$ with 7-carbon (7C), 9-carbon (9C), and 11-carbon (11C) prenylsurfactants [(CH₃)₂C=CH(CH₂)_nSO₃- Na⁺ (n = 4, 6, 8)], is now described where the perepoxide (TS *and/or* intermediate) contributes on a continuum to hydroperoxidation depending on the gaseous or solvated "arrival" of ${}^{1}O_{2}$ to the air—water interface (Figure 1).

Our experiments used two reactors, one of which is a photoreactor, and the other a chemical bubbler, wherein ${}^{1}O_{2}$ is delivered mainly via gas and solution phases to an air—water interface, respectively. The photo- and bubbling-reactors offer a unique way to probe the 'ene' reaction mechanism of ${}^{1}O_{2}$ at the air—water interface. We hypothesized that by using the air—water interface, the continuum between the two mechanistic extremes of a perepoxide TS vs intermediate will be accessed. Thus, the air—water interface was sought as a novel way to discriminate between concerted and stepwise mechanisms on delivery origin of ${}^{1}O_{2}$ to a surface from mainly an upper drier state vs a lower wetter state.

In an effort to accomplish this, methods were required to deliver ¹O₂. First, a photoreactor was used that isolated the photosensitizer away from the solution to avert type I photooxidation

processes that generated *non*-¹O₂ species, such as O₂^{•-}, HO•, and ROO•.^{9,10} The photoreactor provided the transmission of ¹O₂ from the upper sensitizer wafer to the air—water interface. Second, ¹O₂ was generated by the chemical reaction of hydrogen peroxide and KOH with chlorine gas bubbled into the solution. This bubbling reactor led to chemically generated ¹O₂, initially formed as a solvated species.

Previous studies have also examined ${}^{1}O_{2}$ transfer in silicas, zeolites, supramolecular systems, and superhydrophobic surfaces. ${}^{11-16}$ Flow reactors for ${}^{1}O_{2}$ generation and reactions in water are emerging and showing good potential, 17 as well as surfactants ${}^{18-22}$ in reactive oxygen species (ROS) reactions at the air—water interface. ${}^{23-28}$ A study of Singleton et al. 3 on the reaction of *cis*-2-butene and tetramethylethylene with ${}^{1}O_{2}$ proposed a two-step no-intermediate pathway, and laid the groundwork for potential bifurcations on the ${}^{1}O_{2}$ reaction surface. The *trans*-cyclooctene/ ${}^{1}O_{2}$ 'ene' reaction ${}^{29-31}$ is unique in that its allylic hydrogens are inaccessible so that a minimum develops on the potential energy surface (PES) for the perepoxide. The perepoxide intermediate from the *trans*-cyclooctene/ ${}^{1}O_{2}$ reaction was predicted by density functional theory (DFT) and trapped experimentally by triphenylphosphite to form *cis*-epoxide, *trans*-epoxide, triphenylphosphate, and other products. Other ${}^{1}O_{2}$ 'ene' reactions also evidence of trapping of a perepoxide intermediate with formation of epoxides, ${}^{32-34}$ instead of proceeding by a perepoxide TS.

In this paper, we report on an air—water interfacial ${}^{1}O_{2}$ reaction of alkene surfactants to deduce a possible perepoxide TS-to-intermediate continuum. Figure 2A depicts the top-down approach of ${}^{1}O_{2}$ to the air—water interface and its reaction with 7C, 9C, and 11C (eqs 1-4). Figure 2B depicts the bottom-up approach of ${}^{1}O_{2}$ to the air—water interface and its reaction with the same surfactants (eqs 5-7). We sought to address the following questions: (i) Does ${}^{1}O_{2}$ originating as a

gas or in water differ in alkene surfactant oxidation at the air—water interface? (ii) Does a mechanistic difference exist for the oxidation of an alkene surfactant when ${}^{1}O_{2}$ is delivered as an airborne species vs solvated state? (iii) Are the regioselectivity and percent yield of the singlet oxidation affected? (iv) What insight can gas and aqueous phase DFT calculations provide on possible borderline perepoxide TS and intermediate mechanisms?

Figure 1. Alkene surfactants (7C, 9C, and 11C) were used to probe the 'ene' reaction of ${}^{1}O_{2}$ at the air—water interface using photoreactor and bubbling devices. The mechanism is proposed to lead to a perepoxide transition state (TS) in the dry state above the air—water interface (path a), and a perepoxide intermediate near the air—water interface or in the aqueous phase (path b), prior to the formation of secondary (2) and tertiary (3) hydroperoxides.

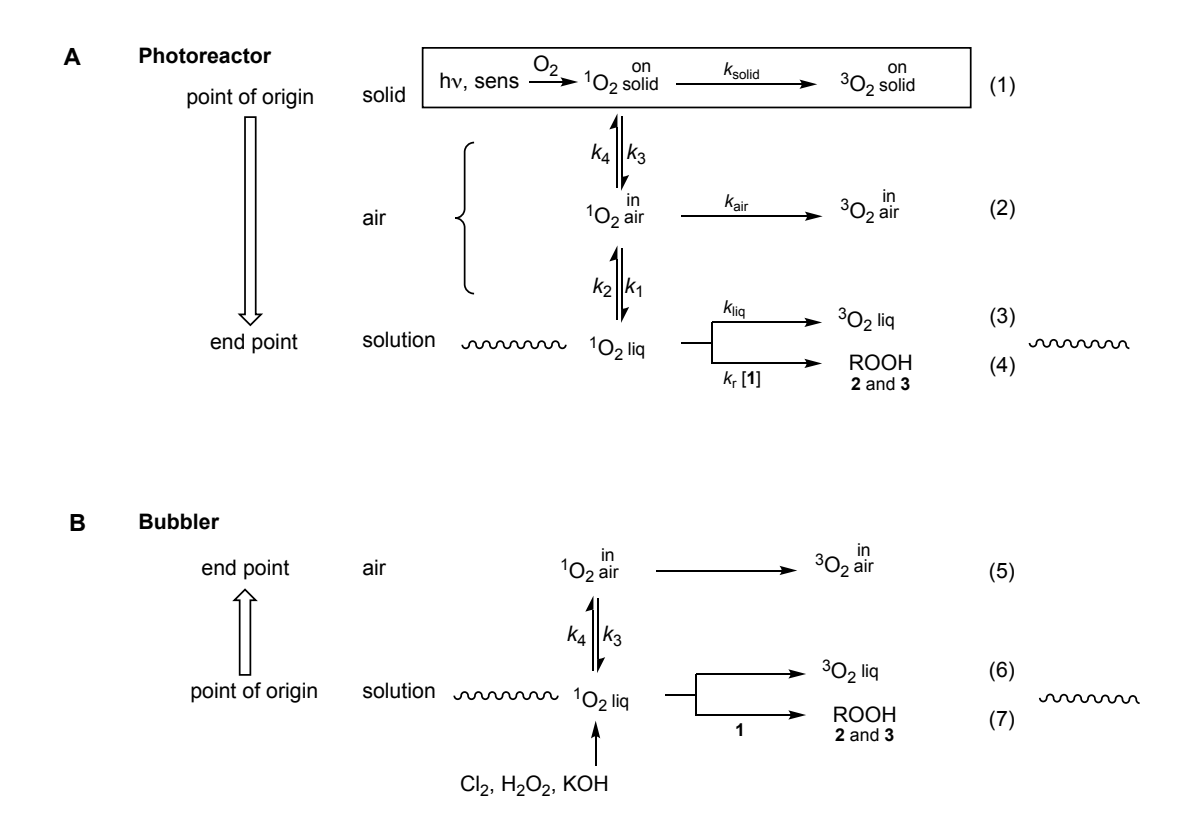


Figure 2. (A) A photoreactor *top-down* delivery of ${}^{1}O_{2}$ to the air–water interface. We show the formation of ${}^{1}O_{2}$ at the sensitizer solid and its physical quenching (eq 1), diffusion through air and its physical quenching in air (eq 2) or by the water surface (eq 3), and chemical reaction with prenylsurfactants 7C, 9C, and 11C to form 7-hydroperoxy-8-methylalkyl-8-ene-1-sulfonate **2** and (*E*)-8-hydroperoxy-8-methylalkyl-6-ene-1-sulfonate **3** (eq 4). For the photoreactor, the surfactant traps ${}^{1}O_{2}$ via gaseous point of origin and then reaches the air–water interface. (B) *Bottom-up* approach of ${}^{1}O_{2}$ to the air–water interface. Singlet oxygen was chemically generated by the reaction of ${}^{1}O_{2}$ with ${}^{1}O_{2}$ in KOH solution and transported to the surfactant solution by bubbling for a reaction with 7C, 9C, and 11C to form **2** and **3**, leading to a reaction both in solution and at the air–water interface.

Experimental

General. Acetone, 9,10-anthracene dipropionate dianion (ADPA), aluminum (III) phthalocyanine chloride tetrasulfonic acid (AlPcS), benzoic acid, Cl₂ gas (≥99.5%), CDCl₃, D₂O (99.8%), dichloromethane (DCM), diethyl ether, *N*,*N*-dimethylformamide (DMF), DMSO-*d*₆ (99.5%), ethanol, ethyl acetate, H₂O₂ (35 wt%), helium (5 ultra-high purity), and porous Vycor glass (Corning 7930 porous, sized 1.0 mm × 2.25 cm²) were obtained commercially and used as received. A deionization system was used to purify water. The syntheses of surfactants 7C and 9C were each carried out in 3 steps in overall yields of 16-27% and purities of 95%, using methods reported in our previous work.³⁵ The synthesis of sodium 10-methylundec-9-ene-1-sulfonate (11C) was carried out in three steps by slightly modifying our previously reported procedure³⁵ in an overall yield 100 mg of 60% and purity of 95%. A facet of the photoreactor and bubbling reactor study is that unless otherwise noted submicellar concentrations of the 7C, 9C, and 11C were used, in which no micelles are present in solution.

Photoreactor. The photoreactor consisted of a shortened quartz cuvette with a size of 0.7 cm × 1.0 cm². H₂O or D₂O (0.60 mL) was placed in the photoreactor that contained either 7C, 9C, or 11C in various amounts. A 0.5 g porous Vycor glass lid of the size 1.0 mm × 2.25 cm² was placed on top of the cuvette. AlPcS (5.0×10^{-6} mol) was coated onto the bottom face of the glass lid. This glass lid generates airborne ${}^{1}O_{2}$ on its bottom face which traveled a 0.4 mm distance relative to the cuvette walls, and a 1.5 mm distance relative to the deepest point of the meniscus, as measured using a digital ruler. The end of a fiber optic was placed 3.0 cm above the glass lid. The fiber optic delivered light from two different laser sources, in which there was a Gaussian distribution of the incident photons. (i) The $k_{\rm T}$ rate constants for the reaction of airborne ${}^{1}O_{2}$ with 7C, 9C, and 11C at the air–D₂O interface were examined at 26 °C by irradiation from Surelite

pulsed Nd:YAG laser using 355-nm light that was connected to a Hamamatsu NIR detector to observe the 1270 nm phosphorescence signal of ${}^{1}O_{2}$. A 1270 nm band-pass filter with a FWHM of 15 nm was used prior to this phosphorescence signal reaching the NIR detector. The lifetime of ${}^{1}O_{2}$ (τ_{Δ}) as a gaseous species and at the air- $D_{2}O$ interface was determined with a least-squares procedure for the curve-fitting. (ii) A continuous wave diode laser was also used with a 669-nm light output (dose = 1400 J/cm²). For both (i) and (ii), the 355-nm and the 669-nm laser outputs overlap well with the AlPcS sensitizer adsorbed on the glass lid. In both cases, airborne ${}^{1}O_{2}$ was generated on the bottom face of the lid, and proceeded over the air gap to the water interface.

Bubbling Reactor. For the bubbling reactor, singlet oxygen was generated on the basis of a chemical reaction of $H_2O_2 + Cl_2 + 2KOH \rightarrow O_2 (\sim 85\% X_3\Sigma g^- \text{ and } \sim 15\% \text{ a}^1\Delta_g) + 2KCl + 2H_2O$ that has been reported previously. 36,37 Briefly, 10.5 mL of 8 M KOH was added to 20 mL of 35 wt% aqueous H₂O₂ in a glass sparger that was immersed in a chiller held at -17.9 °C. The reaction was mixed with Cl₂ (4.99 mL/min) and He (96 mL/min) with a Matheson gas proportioner and then bubbled through the H₂O₂/KOH slush. All of the Cl₂ was reacted with H₂O₂. The gaseous products passed through a cold trap (kept at -70 °C) to remove the water vapor. Only ¹O₂, ³O₂, and He remained in the downstream gas. The concentration of ¹O₂ in the gas was determined by measuring the ${}^{1}O_{2}$ emission (a ${}^{1}\Delta_{g} \rightarrow X_{3}\Sigma g^{-}$, $\nu = 0-0)^{38}$ at 1270 nm in an optical emission cell. Emission from the cell was collected using a plano-convex BK7 lens (f = 30 mm), passed through an optical chopper (SRS model SR540, Sunnyvale, CA, USA) and 5-nm bandwidth interference filter centered at 1270 nm (Andover, blocked to 1550 nm), and focused by another plano-convex BK7 lens (f = 50 mm, AR coated for 1050–1620 nm) into a thermoelectrically cooled InGaAs photodetector (Newport model 71887 detector and 77055 TE-cooler controller, Irvine, CA, USA) coupled with a lock-in amplifier (SRS model SR830, Sunnyvale, CA, USA).

After passing the emission cell, ${}^{1}O_{2}$ (mixed with ${}^{3}O_{2}$ and He) was bubbled into 10 mL of 1 \times 10⁻⁴ M 11C surfactant in a reaction vessel. The solution of 11C was prepared in pure D₂O, pure H₂O, or as D₂O/H₂O mixtures in a volume ratios of 3:1, 1:1, or 1:3. During the experiment, the entire apparatus (including the ${}^{1}O_{2}$ generator and reaction vessel) was continuously pumped using a mechanical pump, and the pressure of the apparatus was maintained at 26 Torr (slightly above the water vapor pressure at room temperature) through a pressure relay (Cole-Parmer 00244OW, Vernon Hills, IL, USA). The pumping served several purposes: reduces the residence time of ${}^{1}O_{2}$ in the gas phase, thus minimizing its wall quenching and self-quenching, and removed O₂, thus replenishing fresh ${}^{1}O_{2}$ to the reaction solution. Because of the low pressure within the reaction vessel, a significant amount of solvent evaporated from the reaction solution and was removed by the vacuum pump. Fresh solvent (with the same D₂O/H₂O composition as the original solution) was replenished into the reaction vessel using an Ismatec Reglo-CPF rotary piston pump (Glattbrugg, Switzerland) at a precisely controlled flow rate, so that the total volume of the solution remained constant throughout the reaction.

In the experiment, chemically generated ${}^{1}O_{2}$ was continuously bubbled into the aqueous solution in the reaction vessel. Singlet oxygen has a longer lifetime in the interior of bubbles (because of reduced encounters with water) than in the bulk solution. After diffusing into the bulk water, ${}^{1}O_{2}$ has a lifetime of \sim 4 µs and can travel only \sim 150 nm. 39,40 Therefore, ${}^{1}O_{2}$ reactions occurred both at the gas–liquid interface of bubbles and in the bulk solution. ADPA was used as a ${}^{1}O_{2}$ trap to estimate the average [${}^{1}O_{2}$] in solution. ADPA is known to react with ${}^{1}O_{2}$ chemically (i.e., without physical quenching), producing endoperoxide via [4 + 2] cycloaddition accompanied by bleaching of the absorption of ADPA. 41 The pH of the ADPA solution (0.05 mM) was maintained at 10 using borax/NaOH buffer. A linear relationship between $ln(A_{1}/A_{0})$ and reaction

time was observed,³⁷ where A_t and A_0 are the ADPA peak absorption (at 378 nm) at different reaction times and time zero, respectively. This indicates that the consumption of ADPA obeys first-order rate law. Using the literature value of reaction rate constant k_r (8.2 × 10⁻⁷ M⁻¹ s⁻¹) for ADPA + 1O_2 , the average concentration of 1O_2 in solution was determined to be \sim 5–7 × 10⁻¹² M. During each experiment, the emission of airborne 1O_2 was continuously monitored, and its variation was controlled to be within 10%. It was found that the average signal output of the emission detector linearly correlates with the ADPA-calibrated [1O_2] in solution. Therefore, in the experiment of 11C surfactants with 1O_2 , the [1O_2] in water was determined based on a calibration curve for the gas-phase emission intensity vs solution-phase concentration.

Computations Details. DFT electronic structure calculations were performed using B3LYP coupled with the 6-31+G(d) basis set. Geometries of reactants, TSs, intermediates and products were fully optimized by calculating force constants at every step. TSs were verified as first-order saddle points by frequency calculations, and the vibrational mode with the imaginary frequency corresponds to the reaction coordinate. Intrinsic reaction coordinate calculations were carried out to further verify that each TS was connected to the correct reactant/product minima. Reaction enthalpies reported for each pathway included thermal corrections at 298 K, for which the zero-point energies were scaled by a factor of 0.9804.⁴² The reactions in aqueous solution were calculated using the SMD solvation model.⁴³ For relaxed PES scan, all bond lengths and bond angles were fully optimized at each step, except for the two scanning reaction coordinates which were each varied continuously from 2.5 to 1.4 Å at a step size of 0.1 Å.

One challenge in the DFT calculations concerns the multiconfigurational ${}^{1}O_{2}$ wave function that mixes open- and closed-shell characters.⁴⁴ The spin-restricted DFT is incapable of treating static correlation arising from the two degenerate π^{*} antibonding orbitals and

overestimates the ¹O₂ excitation energy, while the broken-symmetry, spin-unrestricted DFT brings about spin contamination from ³O₂. The problem exists not only in the ¹O₂ reactant and but may also affect the loosely bonded O₂-adducts (such as a reactant-like precursor complex without a covalent bond and with a large amplitude of intermolecular motions).⁴⁵ To assess the influence of spin contamination on the reaction PES, the B3LYP/6-31G+(d)-optimized ¹O₂ and O₂-adduct structures were subjected to a T1 diagnostic of Lee and Taylor⁴⁶ using the domain-based local pairnatural orbital coupled-cluster single-, double- and perturbative triple-excitation method⁴⁷ DLPNO-CCSD(T) coupled with the aug-cc-pVTZ basis set, wherein $T_1 = t_1/\sqrt{n}$ (i.e., the Frobenius norm of the single-excitation amplitude vector divided by the square root of the number of electrons correlated). The inclusion of a perturbative correction for triple excitation in CCSD(T) compensated for the deficiencies of a single-determinant reference to some extent. Empirically, a T1 value that is greater than 0.02 for a closed-shell system or greater than 0.03 for an open-shell system indicates severe multiconfigurational characters or nondynamical correlation effects. For all reactive structures including ¹O₂, the T1 values do not exceed 0.018. Accordingly, spin contamination does not appear to be a significant issue for the present reaction system. DFT calculations were carried out using Gaussian 09.48 DLPNO-CCSD(T) calculations were conducted by using ORCA 4.2⁴⁹ at a Linux computational cluster equipped with 20 nodes of dual Intel Xeon 28-core 2.7 GHz processors.

Results and Discussion

Apparatus. Two apparatuses were used to probe the 'ene' reaction of ${}^{1}O_{2}$ at the air–water interface as shown in Figure 3. First, an apparatus previously described 35,50–51 was equipped with a porous glass wafer coated with Al(III) phthalocyanine chloride tetrasulfonic acid as the sensitizer

on its bottom face, and a reactor loaded with surfactant on the solution was irradiated from above with red light via an optical fiber. Singlet oxygen traverses an air-gap distance of 0.4 mm from the sensitizer plate to the water surface at the walls of the cuvette and further to the meniscus. Second, a bubbling system previously described^{36,37} led to ${}^{1}O_{2}$ by a chemical reaction of Cl_{2} gas with $H_{2}O_{2}$ in a basic solution. Here, much of the ${}^{1}O_{2}$ was distributed through the water via bubbles. Next, the results from the use of these two techniques are presented.

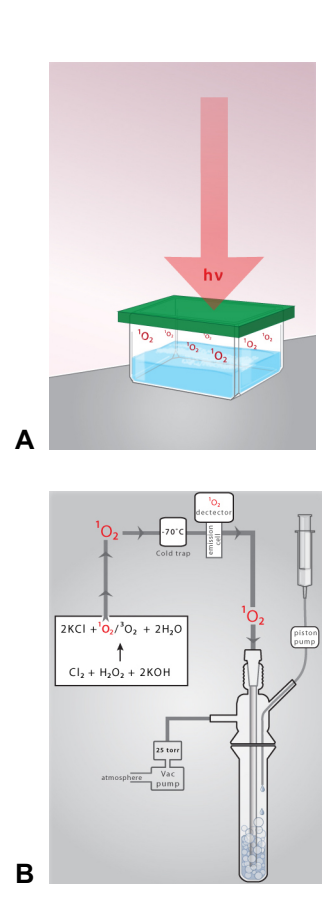


Figure 3. (A) *Top-down* approach of the photoreactor with delivery of ${}^{1}O_{2}$ to the air–water interface. (B) *Bottom-up* approach of ${}^{1}O_{2}$ to the air–water interface with the chemical generation of ${}^{1}O_{2}$.

The results are presented as follows: (1) the total quenching rate constants (k_T) for the removal of ${}^{1}O_{2}$ by the surfactants; (2) analysis of the device geometry on hydroperoxide product yield; (3) the regioselectivity of hydroperoxides based on chain length; (4) effect of solvent deuteration; (5) the sorting out of DFT computed gas- and water-phase contributions to the ${}^{1}O_{2}$ 'ene' reaction; and (6) mechanistic considerations.

Effect of Chain Length on $k_{\rm T}$. With the advent of a technique to monitor the quenching of ${}^{1}O_{2}$ at the air- $D_{2}O$ and air-solid interfaces, 16,51 the rate constants k_{T} can show the removal of ${}^{1}O_{2}$ by the surfactants. In the present k_{T} experiments, the use of $D_{2}O$ was preferred due to longer lifetime in D₂O (τ_{Δ} = 66 µs) than in H₂O (τ_{Δ} = 4.5 µs),⁵² thereby facilitating the time-resolved measurements. Consequently, surfactants 7C, 9C, and 11C provide the first opportunity to measure the removal of ¹O₂ to assess chain length on the rate constant at the air-water interface. The interfacial effect on the $k_{\rm T}$ of ${}^{1}{\rm O}_{2}$ was measured by monitoring the ability of alkene surfactants 7C, 9C, and 11C to quench the phosphorescence of ¹O₂ at 1270 nm as shown in eq 4 (Figure 2). Of the two decay components observed in the 1270 nm ${}^{1}O_{2}$ phosphorescence, there was a slow component corresponding to ¹O₂ in the air space and a fast component ascribed to ¹O₂ at the air–D₂O interface, respectively. The $k_{\rm T}$ of ${}^{1}{\rm O}_{2}$ of 9C was previously measured to be $1.1 \times 10^{6} \, {\rm M}^{-1} \, {\rm s}^{-1}$ at the air/liquid interface. 51 We find that quenching of the phosphorescence of 1O2 at the air/D2O interface produces $k_{\rm T}$ values that are increased by 2.7-fold for 11C compared to 9C, and 4.6-fold for 11C compared to 7C (Figure 4 and Table 1). These interfacial k_T values are similar to homogenous solution k_T values reported for trisubstituted alkenes, 53,54 in which increasing the surfactant chain length, from 7C to 11C, increased not only the $k_{\rm T}$ of $^{1}{\rm O}_{2}$ for the prenylsurfactants, but also the percent yield of hydroperoxides from 'ene' reactions, as we will see next.

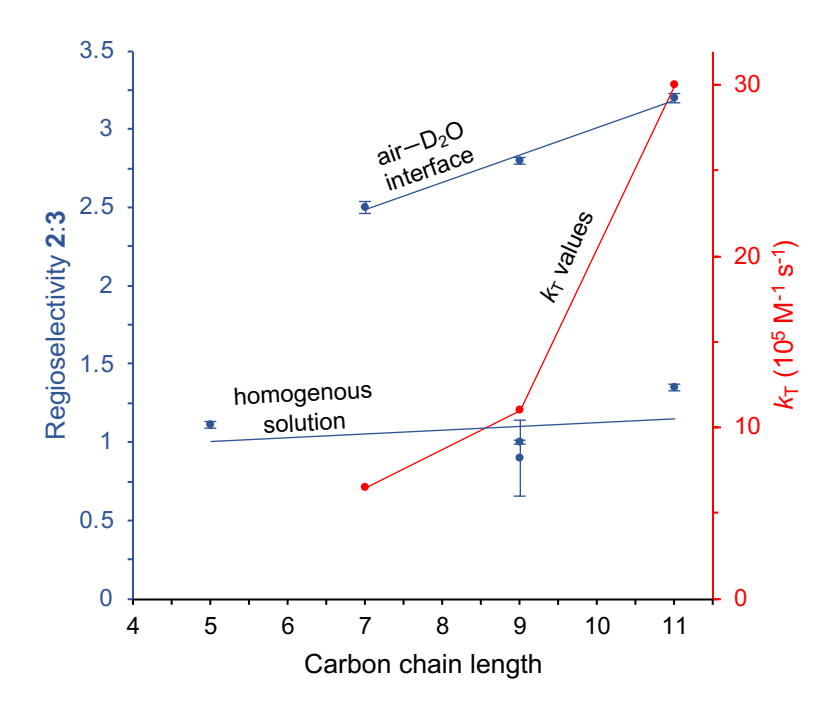


Figure 4. A plot of regioselectivity in forming **2**:3 (upper • trendline y = 0.175x + 1.26, R² = 0.993) and total quenching rate constant k_T (•) vs alkene chain length of surfactants 7C, 9C, and 11C upon delivery of ${}^{1}O_{2}$ to the air−D₂O interface. Regioselectivity in forming **2**:3 (lower • trendline y = 5.87x - 37.0, R² = 0.0908) alkene chain length, and surfactants 9C and 11C of ${}^{1}O_{2}$ in homogeneous solution CD₃CN/D₂O (9:1). The k_T of 2-methyl-2-pentene is taken from ref. 53.

Table 1. Effects of Surfactant Mixing on Percent Yield and Ratio of Hydroperoxides 2 and 3 Formed by Ene $^1\mathrm{O}_2$ Reactions

entry	compound	method		$^{1}\mathrm{O}_{2}$		% yield	product	
		carbon chain length	solvation state	interfacial	solvent	(2+3)	ratio 2/3	$k_{\mathrm{T}} \ \mathrm{M}^{-1} \mathrm{s}^{-1}$
1 ^a	undecene- sulfonate	11	¹ O ₂ air-water not solvated	**************************************	$\mathrm{D}_2\mathrm{O}$	85 ± 2 °	3.2 ± 0.03 °	3.0 × 10 ⁶
2 ª	nonene- sulfonate	9	¹ O ₂ air–water not solvated	¹ O ₂	$\mathrm{D}_2\mathrm{O}$	81 ± 2 °	2.8 ± 0.02 °	1.1 × 10 ^{6, d}
3 a	heptene- sulfonate	7	¹ O ₂ air–water not solvated	liquid	D ₂ O	75 ± 3 °	2.5 ± 0.04 °	6.5 × 10 ⁵

4 ^b	undecene- sulfonate	11	¹ O ₂ solvated	liquid	D ₂ O	67.4 ^e	1.35 ± 0.02	-
5 ^b	undecene- sulfonate	11	¹ O ₂ solvated	air	D ₂ O:H ₂ O 3:1	64.3 ^e	1.04	-
6 ^b	undecene- sulfonate	11	¹ O ₂ solvated	¹O ₂	D ₂ O:H ₂ O 1:1	54.9 °	1.30	-
7 ^b	undecene- sulfonate	11	¹ O ₂ solvated	↑ ¹O ₂ ↑	D ₂ O:H ₂ O 1:3	42.5 °	1.34	-
8 ^b	undecene- sulfonate	11	¹ O ₂ solvated	10 ₂ 10 ₂ 10 ₂	H ₂ O	31.3 °	1.31	-
9 5	nonene- sulfonate	9	micelle	102 air	H ₂ O	25 ± 6	0.9 ± 0.2	-
10 ^g	nonene- sulfonate	9	solvated	¹ O ₂ ¹ O ₂	aqueous CD₃CN	100 ± 1	1.0 ± 0.01	-

^a Airborne ¹O₂ was generated by the photoreactor for 1 h. Samples of 1 mM surfactant were in 0.6 mL D₂O (submicellar concentration). ^b Bubbler introduced ¹O₂ from a reaction of Cl₂, H₂O₂ and KOH for 1 h. Samples of 1 mM surfactant in 3 mL (submicellar concentration). ^c Ref. 35. ^d Ref. 51. ^e Errors are ±1%. ^f Airborne ¹O₂ was generated by the photoreactor for 1 h. Samples of 25 mM surfactant were in 0.6 mL H₂O (micellar concentration). ^g Airborne ¹O₂ was generated by the photoreactor for 1 h. Samples of 1 mM surfactant were in 0.6 mL CD₃CN/D₂O (9:1).

Effect of Device Geometry on Hydroperoxide Product Yield. The percent yield of the hydroperoxide products 2 and 3 was investigated based on configurations of the ¹O₂ apparatus. Table 1 shows the results that were collected for the photoreactor (entries 1-3, 9 and 10) and bubbler (entries 4-8) systems. For the photoreactor with D₂O, as the surfactant chain length increases from 7C to 11C, an increase in hydroperoxide percent yield from 75% to 85% was observed. The percent yield of hydroperoxides for 11C in the photoreactor was 85% and in the bubbler was 67.4% (cf. entries 1 and 4); this reduction is attributed to greater solvation in the latter. The effect of solvent deuteration is evident in the bubbler reactor, the hydroperoxide percent yield was decreased from 67.4% in D₂O to 31.3% in H₂O (cf. entries 4 and 8). For the photoreactor, 11C in a micellar condition shows a loss of the regioselectivity (entry 9), suggesting that the reaction of airborne ¹O₂ reaches the water phase, which then enters a hydrophobic core similar to homogeneous phase. Arrival of airborne ¹O₂ to a solution interface with alkene surfactant sites solvated also in "on water/CD₃CN" organic reaction (entry 10), also led to a loss of regioselectivity indicating the need for the interaction of ¹O₂ with the alkene site positioned above the air-water interface (entries 1-4). The regioselectivity of the surfactant-¹O₂ 'ene' reaction was also investigated based on the ¹O₂ apparatus, as described next.

Effect of Chain Length on Regioselectivity of the 'Ene' Reaction. The prenylsurfactants reacted with ${}^{1}O_{2}$ to give two 'ene' hydroperoxides 2 and 3 in varying ratios. For the photoreactor, the product ratios of 2:3 decreased from 3.2 ± 0.03 for 11C, to 2.8 ± 0.02 for 9C, and to 2.5 ± 0.04 for 7C (entries 1-3). The regioselectivity is all but lost in the bubbler compared to the photoreactor. For the bubbler reactor, the regioselectivity ranged from 1.35:1 to 1.04:1 (entries 4-8). The micelle or solution phase ranged from 0.9:1 to 1.11:1 (entries 9-11). There is little or no regioselectivity in the solvated state. In homogeneous solution, ${}^{1}O_{2}$ 'ene' reactions show little or no preference, where

2 and **3** are formed in nearly equal amounts. A complete loss of regioselectivity when 9C is dissolved in a homogeneous solution, as has been observed for 2-methyl-2-pentene in organic solvents (entries 10 and 11). Next, our analysis shows the reactivity of 11C with ${}^{1}O_{2}$ with various compositions of $D_{2}O$ vs $H_{2}O$.

Effect of Solvent Deuteration. Experiments were conducted to quantitate the percent yield of hydroperoxides 2 and 3 in the reaction of 11C. Table 1 shows that the percent yield of the hydroperoxides increased by ~2-fold in D₂O compared to H₂O (67.4% in D₂O and 31.3% in H₂O, entries 4 and 8). We find that 11C's chemical reactivity does not increase by 20-fold as would be expected for aqueous solvated species with the known longer ¹O₂ lifetime in D₂O compared to H₂O.⁵² For fully solvated ¹O₂, the lifetime increase by 15-fold from H₂O to D₂O would have been expected to dramatically increase product yield in the latter. Thus, the results are consistent with the partial solvation of 1 and point to a dependence on mixing rates, as will be seen next.

Effects of Gas and Water Phases Based on DFT Calculations. Gas-phase calculations wherein all structures are dry. When ${}^{1}O_{2}$ attacks the 11C surfactant in a cis orientation in the gas phase, a perepoxide structure forms as a TS (Figure 5a). The reaction follows Singleton and coworkers' two-step no-intermediate mechanism.³ Both TS1 and TS2 in Figure 5a are located in energy below the reactants. The energy gap between TS1 and TS2 is 12 kJ/mol calculated at B3LYP/6-31+G(d). Singlet oxygen attacks the π bond nearly symmetrically, as shown by the close distances of R2 and R3 in TS1 (R2 = 2.07 Å and R3 = 2.16 Å). The 2° hydroperoxide is a less stable anti-Markovnikov product, while the 3° hydroperoxide is a more stable Markovnikov product. According to the 2D-PES shown in the top left frame of Figure 6, a longer route is required to reach the 2° ROOH compared to that for the 3° ROOH. For comparison of the reaction of 11C with that of a short-chain species, the PES for the ${}^{1}O_{2}$ reaction with 2-methyl-2-butene in the gas

phase was calculated as well. It also shows a two-step no-intermediate process, consistent with the results of Singleton et al.³ The perepoxide complex could also be characterized as a loosely bound perepoxide when ¹O₂ attacks the 11C surfactant in a *trans* orientation. As shown in Figure 5b, the binding strength of such a ¹O₂ complex is 32 kJ/mol at B3LYP/6-31+G(d). Considering that the B3LYP calculation may be affected by the spin contaminations arising from the ¹O₂ reactant and its adducts, we have refined the gas-phase reaction energetics using the domain-based local pair-natural orbital coupled-cluster single-, double- and perturbative triple-excitation method⁴⁷ with DLPNO-CCSD(T) coupled with the aug-cc-pVTZ basis set. The inclusion of a perturbative correction for triple excitation in CCSD(T) enables to some extent a compensation for the deficiencies of a single-determinant reference. The corrections of the PES energies at the CCSD(T) level of theory are overall minor. The major revision by the CCSD(T) theory is that the gas-phase transition states TS1 and TS2 for the gas-phase *cis* reaction are both below the starting reactants, while the TS3 for the gas-phase *trans* reaction raises up to 2 kJ/mol above the starting reactants. This rationalizes (to some extent) the experimentally observed the *cis*-effect.⁵

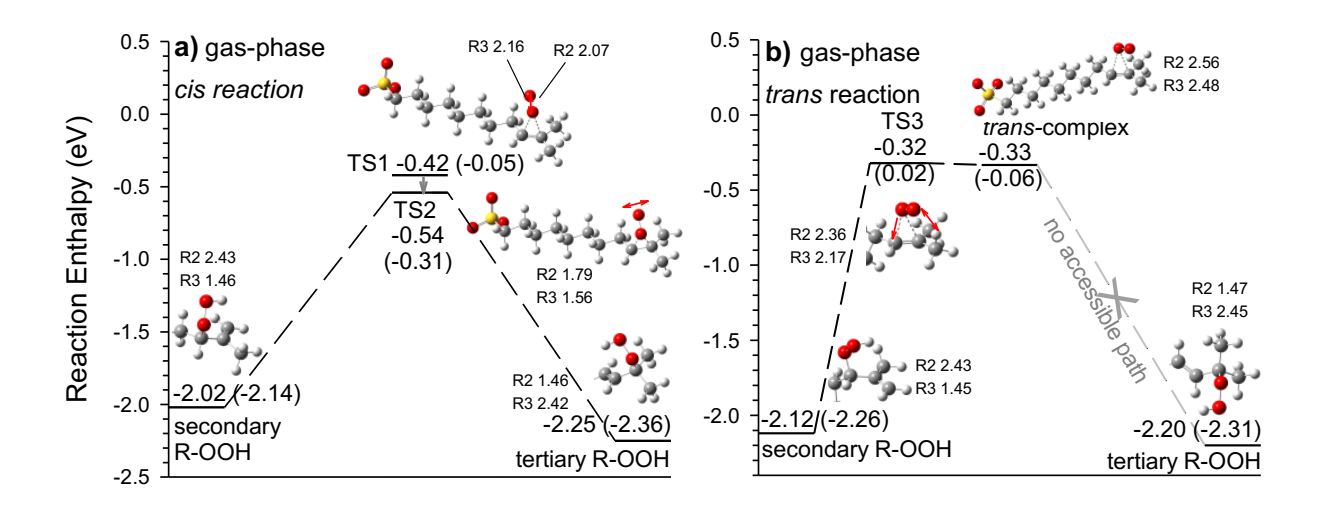


Figure 5. Reaction coordinates for the ${}^{1}O_{2}$ oxidation of 11C surfactant in the gas phase, occurring in (a) a *cis*-orientation and (b) a *trans*-orientation, respectively. Reaction enthalpies (relative to the corresponding reactants) were calculated at B3LYP/6-31+G(d) and DLPNO-CCSD(T)/aug-cc-pVTZ (values listed in parenthesis), respectively, both of which include thermal corrections at 298 K. For most structures, only the portions participating in reactions are depicted. For TSs, vibrational modes corresponding to imaginary frequencies are indicated by displacement vectors. Bond lengths are indicated in the unit of angstrom.

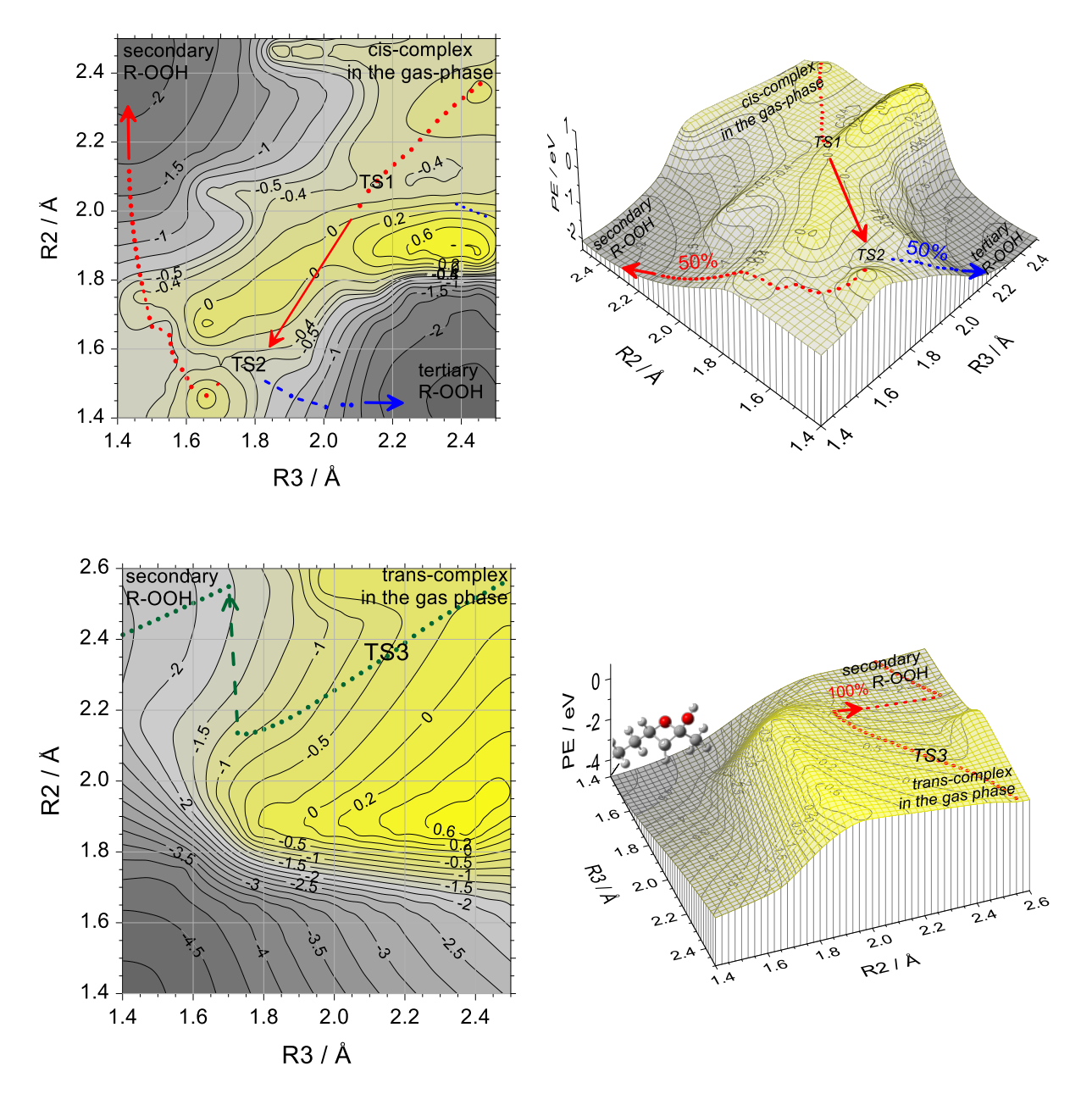


Figure 6. Relaxed 2D-PES scan along the R2 and R3 bond lengths (see definitions in Figure 5) of (top) a *cis*-reaction formed in the gas phase, which leads to the formation of both secondary and tertiary hydroperoxides (indicated by dotted lines) via the same transition state TS2 and thus with equal possibilities; and (bottom) a *trans*-reaction formed in the gas phase, which exclusively

evolves to a secondary hydroperoxide via TS3 (indicated by dotted line). Numbers in the contour map are the potential energies calculated at the B3LYP/6-31+G(d) level of theory.

Water-phase calculations wherein all structures are fully solvated. Different than the gasphase scenario, the perepoxide of the 11C surfactant exists as an intermediate complex in aqueous solution regardless of the ${}^{1}\text{O}_{2}$ -approaching orientations, as shown by 1D reaction PESs in Figure 7 and relaxed 2D-PESs in Figure 8. The binding energies of the *cis-/trans*-perepoxides are 85-88 kJ/mol in water and is more tightly bonded than the gas-phase analogous. The solution-phase reaction follows Acevedo and co-worker's *cis-* and *trans*-perepoxide intermediate mechanism. Note that DFT PES implies that the formation of the 2° ROOH is more favored as it can be formed via both *cis-* and *trans*-perepoxide intermediates. The gas-phase perepoxide TSs have long C-O bonds (R2 = 1.8 – 2.4 Å and R3= 1.6 – 2.2 Å). In contrast, the solvated perepoxide intermediate contains shorter C-O bonds (R2 = 1.5 Å and R3 = 1.6 Å). The latter is anticipated for decreased π -bond character, which is similar to C-O bond lengths of epoxides (~1.47 Å).

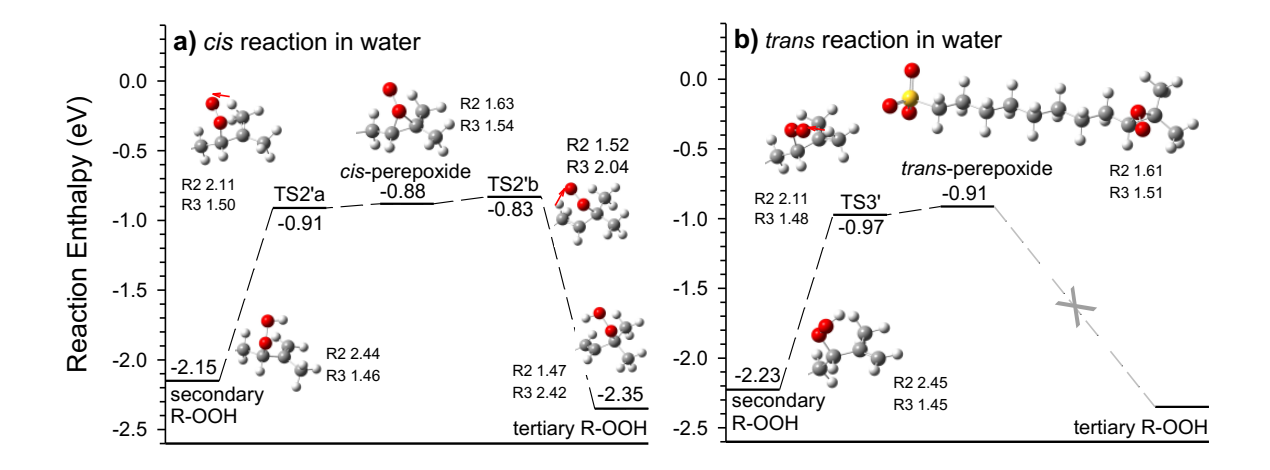


Figure 7. B3LYP/6-31+G(d)-computed reaction coordinates for ${}^{1}O_{2}$ oxidation of 11C surfactant in water, mediated by (a) a *cis*-perepoxide and (b) a *trans*-perepoxide, respectively. Reaction enthalpies are relative to the corresponding reactants, and include thermal corrections at 298 K. Water solvation effects were calculated using the PCM model. For most structures, only the portions participating in reactions are depicted. For TSs, vibrational modes corresponding to imaginary frequencies are indicated by displacement vectors. Bond lengths are indicated in the unit of angstrom.

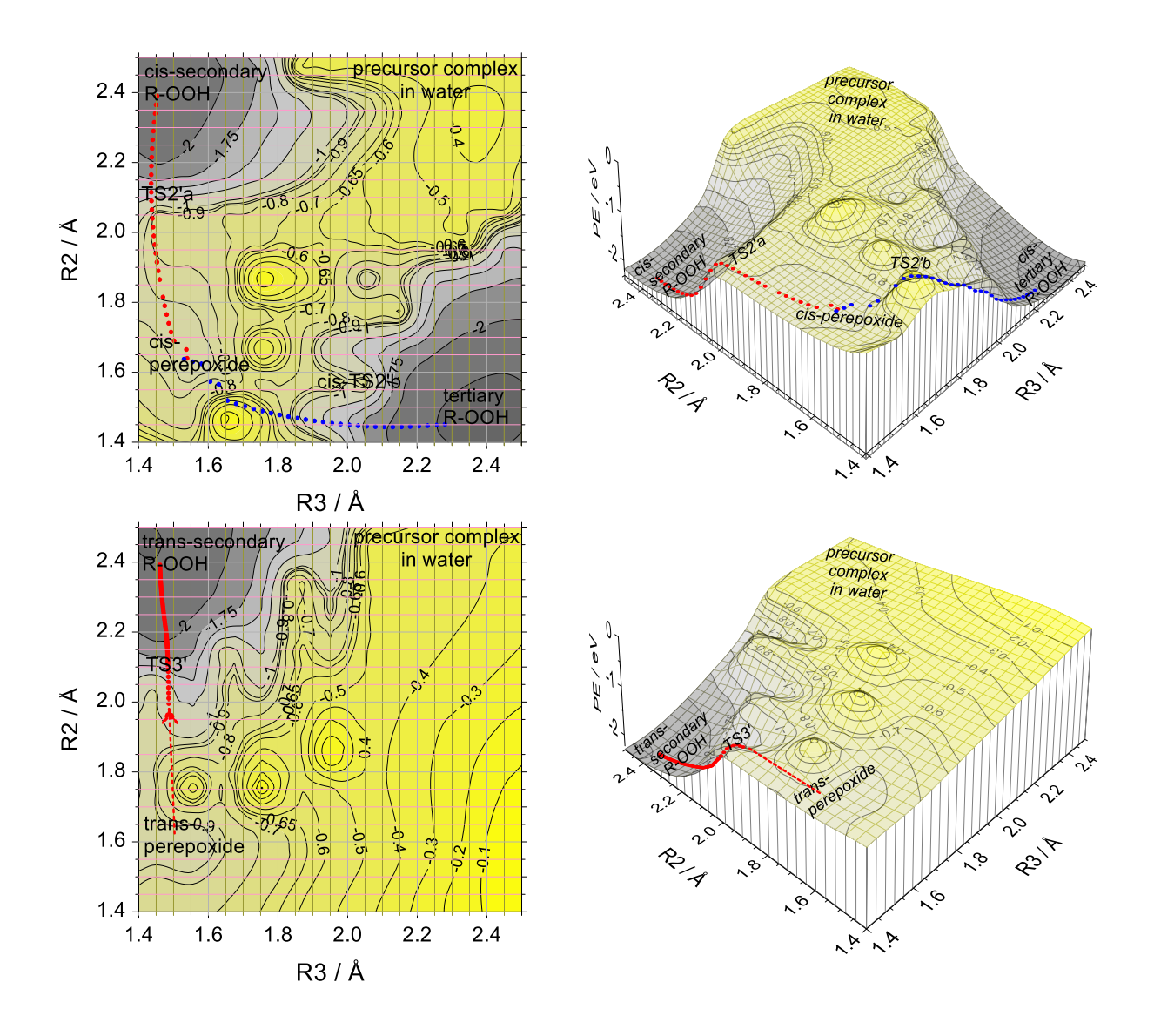


Figure 8. Relaxed 2D-PES scan along the R2 and R3 bond lengths (see definition in Figure 7) of (top) a *cis*-perepoxide formed in solution, which leads to secondary and tertiary hydroperoxides via TS2'a and TS2'b, respectively; the two product channels have nearly equal activation barriers, with the secondary hydroperoxide being slightly favored; and (bottom) a *trans*-complex formed in solution, which evolves exclusively to secondary hydroperoxide via TS3'. Numbers in the contour map are the potential energies calculated at the B3LYP/6-31+G(d) level of theory.

Mechanistic Considerations. The mechanism that we propose is based on an ${}^{1}O_{2}$ interfacial effect in the partitioning of the perepoxide toward a TS or an intermediate. Our DFT computations provide evidence for borderline mechanisms, in which the perepoxide is a transition state in the gas phase while an intermediate in the water phase. These DFT computed results combined with the experimental results in the photoreactor and bubble reactor provide evidence for the formation of perepoxide in a continuum from TS to intermediate. The data with interfacial effects are reminiscent of structure effects provided by strained alkenes in which cases the allylic proton in *trans*-cyclooctene is remote and out of the proper position for abstraction by ${}^{1}O_{2}$ thereby enabling the formation of a perepoxide intermediate. 29,30 The DFT computed initial interaction of ${}^{1}O_{2}$ at the alkene site of 11C is sensitive to the gas phase as the perepoxide TS is very weakly bound with a strength of only 32-41 kJ/mol with long C–O bonds of 1.8 – 2.4 Å. This situation changes in aqueous solution, in which the perepoxide intermediate is bound with a higher strength of 85-88 kJ/mol with shorter C–O bonds of 1.5 – 1.6 Å and bears a resemblance to typical C–O bond lengths of epoxides.

To provide evidence for variable reactivity of ${}^{1}O_{2}$ to the air–water interface, the singlet oxygenations by the photoreactor and bubble reactor in the presence of surfactants were of use. In the photoreactor, higher hydroperoxidation yields were observed as the surfactant length increased. We attributed this increased product yield to the enhanced contact between the alkene group and ${}^{1}O_{2}$ in the air gap from longer surfactants. In the bubble reactor, replacing the solvent $H_{2}O$ for $D_{2}O$ led to a 2.1-fold increase of the reaction yield of 11C, which is less that the 20-fold increase that would be expected when ${}^{1}O_{2}$ is fully solvated. The water O–H bond oscillators^{55,56} can readily quench ${}^{1}O_{2}$ to the ground state ${}^{3}O_{2}$, so that ${}^{1}O_{2}$ migrates only ~150 nm as a solvated species. In the

photoreactor, the unequal abstractions of surfactant methyl and methylene allylic hydrogens provided a further mechanistic handle.

We favor a mechanism shown in Figure 9A for the ¹O₂ 'ene' reaction at the air-water interface. The following mechanisms depicted in Figures 9B-9F are not consistent with our results: (i) attribution of regioselectivity to hyperconjugation⁵⁷ of the alkene head is unlikely due to high energetics for C–C bond/no-bond resonance, (ii and iii) implicit water via electronic repulsion to the perepoxide is unlikely since O-H bonds and not lone pair electrons situate themselves vertically, ⁵⁸ or the water interface as a "large" substituent is unlikely as it would preferentially lead to the 3° hydroperoxide, not the 2° hydroperoxide, as observed, (iv and v) specific water interactions via anchimeric assistance or H-bonding to the perepoxide are unlikely in which the 3° hydroperoxide would be preferred, and not the 2° hydroperoxide, and higher percent yields for shorter surfactant in the series, both opposite to what was observed. The proposed mechanism is in Figure 9A, in which the water layer is functioning as physical quencher of the approaching ¹O₂ is thus proposed as the most likely mechanism, as seen in Figure 2 (eq 3). Vibrational physical quenching of ¹O₂ by water is pertinent here, as reported previously. ^{55,56,59-61} Pertinent here is the higher yield and greater selectivity in the longer chain 11C as it minimizes contact between the prenyl group and water, for preferential allylic hydrogen abstraction of the methyl groups by airborne ¹O₂. The methylene allylic hydrogens are less accessible (closer to the physically quenching water surface), making the methyl hydrogen abstraction favorable to reach the 2° hydroperoxide.

The importance of the surfactant chain length is similarly corroborated by an increase in regioselectivity of the 2° ROOH in longer 11C compared to the shorter 9C and 7C. Singlet oxygen is a longer-lived species in the gas phase for arrival at the surface for an increase in selectivity as

the chain length increases from 7C to 9C then to 11C (from 2.5:1 to 3.2:1). This pattern might reflect a greater aqueous layer influence in the shorter chain surfactants, and accompanying reduction in regioselectivity, which reduces even further in the ${}^{1}O_{2}$ bubbler. For the ${}^{1}O_{2}$ bubbler, the regioselectivity nearly disappears, even for the long chain 11C surfactant (Figure 9G).

This led us to ask the question: *How does the work fit in the field of organic oxidation selectivity?* The work improves the state of the art since delivery of ${}^{1}O_{2}$ from mainly a dry or wet origin can tune the selectivity from high to low. A mechanistic picture is available for turning off regioselectivity in the hydrogen abstraction step of ${}^{1}O_{2}$ with alkene surfactant. In the photoreactor, surfactant molecules are evenly dispersed on the water surface and reside at the interface. In the bubble reactor, a dynamic sparging results, where the attack of ${}^{1}O_{2}$ on surfactant molecules arises in a higher solvated state, and thus regioselectivity is lost, in contrast to the situation with the photoreactor.

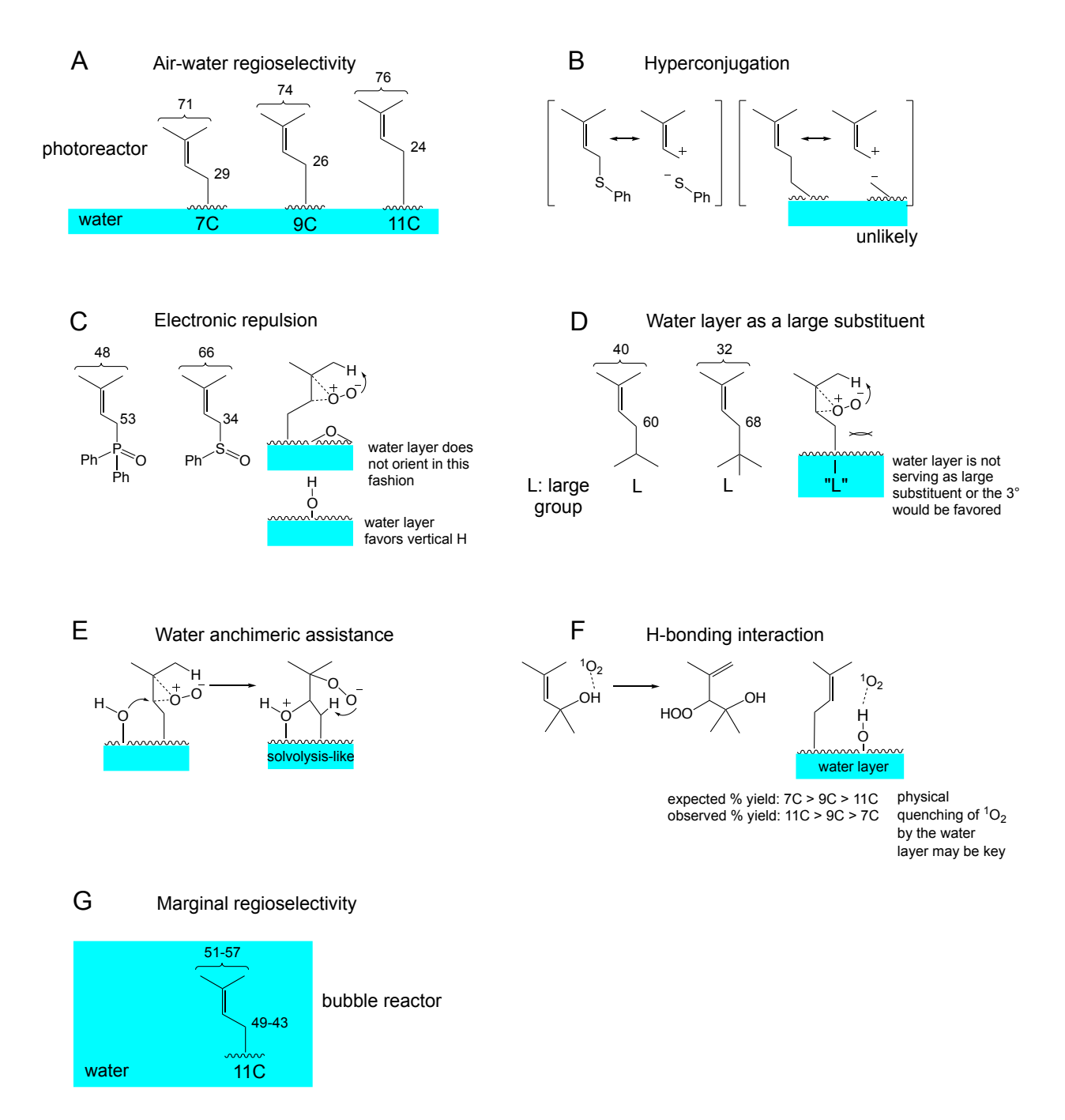


Figure 9. Possible mechanisms to account for the regionselectivity observed in the reaction of surfactants with ${}^{1}O_{2}$ at the air—water interface.

Summary. Many studies have focused on ${}^{1}O_{2}$ chemistry in the solution phase or the gas phase, but sparingly few have focused on ${}^{1}O_{2}$ at the air—water interface, in part due to the need to develop surface-active compounds. Furthermore, reactors for ${}^{1}O_{2}$ generation and reactions in water have yet untapped potential. To make inroads in this vein, two methods and three alkene surfactants (7C, 9C, and 11C) were used to probe the ${}^{1}O_{2}$ 'ene' reaction at the air—water interface. DFT computed results point to solvation differences in a continuum from the gas-phase perepoxide TSs with low binding strengths to the solution-phase perepoxide intermediates with higher binding energies. With the alkene site located further away from the aqueous interface, this harkens us back to the old adage: *location, location, location.* A mechanism is proposed that explains how physically isolated ${}^{1}O_{2}$ and solution-phase ${}^{1}O_{2}$ affect the 'ene' reaction with tunability for the range of the perepoxide as a TS to intermediate. The positioning of the alkene site is key, where regions emerge that controllably react the alkene with dry or wet ${}^{1}O_{2}$.

Conclusion

Photoreactor and bubble reactors were used to provide mechanistic insight in which ${}^{1}O_{2}$ was directionally trapped at the air—water interface. These reactors contained no photosensitizer in solution which was advantageous for enabling singlet oxygen's reactivity to be assessed without intervening species from type I photooxidation reactions. The use of the photo- and bubble-reactors for generation of ${}^{1}O_{2}$ in alkene surfactant oxidations led to the 'ene' reaction of ${}^{1}O_{2}$ and formation of a secondary and tertiary hydroperoxide at the air—water interface. Mechanistic evidence is provided for a continuum of the perepoxide ranging from a TS to an intermediate. Future studies could focus on deuterium labelling one of the two geminal methyl groups for further insight to the regioselectivity of the ${}^{1}O_{2}$ 'ene' reaction under the two experimental conditions

described in this paper. Future studies could also be undertaken including enhanced selective oxidation reactions, further control of the perepoxide TS and intermediate continuum, and comparison of surface area exposed to air with high and low surfactant packing at the air—water interface.

Control of ${}^{1}O_{2}$ chemistry at the air–water interface and airborne state can make the photoreactor and bubble reactor methods advantageous to other methods, such as structure constraints (i.e., inaccessible allylic H) or homogeneous solutions.^{29–31} The tuning of the ${}^{1}O_{2}$ 'ene' process with ${}^{1}O_{2}$ as a gaseous species or partially aqueous solvated species makes these methods relevant for mechanistic control by the air–solution interface and fate of the ${}^{1}O_{2}$ reaction. Such interfacial ${}^{1}O_{2}$ control and mechanism is relevant in air, and oxidative damage, and adds to recent work focusing on other ROS such as HO* and ozone at an air–water interface.^{62–67} The impact of the work goes beyond organic chemistry and is related to biologically relevant models of ${}^{1}O_{2}$ at membrane or marine aerosol surfaces.

ASSOCIATED CONTENT

Supporting Information

Instrumentation and analysis methods; calculation of water layer surface-to-volume (S/V) ratios; an example of the $^{1}O_{2}$ phosphorescence decay trace; DFT computed energies and geometries of stationary points of structures.

AUTHOR INFORMATION

Corresponding Authors

Jianbo.Liu@qc.cuny.edu; AGreer@brooklyn.cuny.edu

ORCID

Belaid Malek: 0000-0002-3034-861X

Wenchao Lu: 0000-0002-3798-5128

Prabhu Prasad Mohapatra 0000-0002-6707-048X

Niluksha Walalawela: 0000-0002-6739-5049

Shakeela Jabeen: 0000-0002-7153-3379

Jianbo Liu: 0000-0001-9577-3740

Alexander Greer: 0000-0003-4444-9099

ACKNOWLEDGMENT

B.M., P.P.M, N.W., S.J., and A.G. acknowledge support from the National Science Foundation (CHE-1856765). W.L. and J.L. acknowledge the support by the National Science Foundation (Grant No. CHE-1856362). This work used Comet and Expanse, in the Extreme Science and Engineering Discovery Environment (XSEDE) cluster at the San Diego Supercomputer Center, which is supported by the NSF (ACI-1548562) through allocation CHE-210052. We also thank Leda Lee for assistance with the graphic arts work.

REFERENCES

- 1. Griesbeck, A. G.; Goldfuss, B.; Jager, C.; Brullingen, E.; Lippold, T.; Kleczka, M. Strong Asymmetry in the Perepoxide Bifurcation Mechanism: The Large-Group Effect in the Singlet Oxygen Ene Reaction with Allylic Alcohols. *ChemPhotoChem* **2017**, *1*, 213-221.
- 2. Ess, D. H.; Wheeler, S. E.; Iafe, R. G.; Xu, L.; Çelebi-Olçum, N.; Houk, K. N. Bifurcations on Potential Energy Surfaces of Organic Reactions. *Angew. Chemie Int. Ed.* **2008**, *47*, 7592-7601.
- 3. Singleton, D. A.; Hang, C.; Szymanski, M. J.; Meyer, M. P.; Leach, A. G.; Kuwata, K. T.; Chen, J. S.; Greer, A.; Foote, C. S.; Houk, K. N. Mechanism of Ene Reactions of Singlet Oxygen. A Two-Step No-Intermediate Mechanism. *J. Am. Chem. Soc.* **2003**, *125*, 1319-1328.
- 4. Ortega, T.; Ozer, G.; Gronert, S.; Erden, I. Singlet Oxygenation of Triquinacene, Barrelene, and Homobarrelene. *Tetrahedron Lett.* **2020**, *61*, 151779.
- Alberti, M. N.; Orfanopoulos, M. Unraveling the Mechanism of the Singlet Oxygen Ene Reaction: Recent Computational and Experimental Approaches. *Chem. Eur. J.* 2010, 16, 9414-9421.
- 6. Sheppard, A. N.; Acevedo, O. Multidimensional Exploration of Valley–Ridge Inflection Points on Potential-Energy Surfaces. *J. Am. Chem. Soc.* **2009**, *131*, 2530–2540.
- 7. Alberti, M. N.; Orfanopoulos, M. The Cyclopropyl Group as a Hypersensitive Probe in the Singlet Oxygen Ene Reaction Mechanism. *Org. Lett.* **2008**, *10*, 2465-2468.
- 8. Grdina, M. B.; Orfanopoulos, M.; Stephenson, L. M. Stereochemical Dependence of Isotope Effects in the Singlet Oxygen-Olefin Reaction. *J. Am. Chem. Soc.* **1979**, *101*, 3111-3112.
- 9. Baptista, M. S.; Cadet, J.; Di Mascio, P.; Ghogare, A. A.; Greer, A.; Hamblin, M. R.; Lorente, C.; Nunez, S. C.; Ribeiro, M. S.; Thomas, A. H.; Vignoni, M.; Yoshimura, T. M. Type I and

- Type II Photosensitized Oxidation Reactions: Guidelines and Mechanistic Pathways. *Photochem. Photobiol.* **2017**, *93*, 912-919.
- Baptista, M. S.; Cadet, J.; Greer, A.; Thomas, A. H. Photosensitization Reactions of Biomolecules: Definition, Targets, and Mechanisms. *Photochem. Photobiol.* 2021, 97, 1456-1483.
- 11. Ramamurthy, V.; Sivaguru, J. Supramolecular Photochemistry as a Potential Synthetic Tool: Photocycloaddition. *Chem. Rev.* **2016**, *116*, 9914-9993.
- Sivaguru, J.; Natarajan, A.; Kaanumalle, L. S.; Shailaja, J.; Uppili, S.; Joy, A.; Ramamurthy,
 V. Asymmetric Photoreactions within Zeolites: Role of Confinement and Alkali Metal Ions.
 Acc. Chem. Res. 2003, 36, 509-521.
- Cojocaru, B.; Laferrière, M.; Carbonell, E.; Parvulescu, V.; García, H.; Scaiano, J. C. Direct Time-Resolved Detection of Singlet Oxygen in Zeolite-Based Photocatalysts. *Langmuir* 2008, 24, 4478-4481.
- 14. Li, X.; Ramamurthy, V. Selective Oxidation of Olefins within Organic Dye Cation-Exchanged Zeolites. *J. Am. Chem. Soc.* **1996**, *118*, 10666-10667.
- Tonon, C. C.; Ashraf, S.; Alburquerque, J. Q.; Nara de Sousa Rastelli, A.; Hasan, T.; Lyons,
 A. M.; Greer, A. Antimicrobial Photodynamic Inactivation Using Topical and
 Superhydrophobic Sensitizer Techniques: A Perspective from Diffusion in Biofilms.
 Photochem. Photobiol. 2021, 97, 1266-1277.
- 16. Durantini, A. M.; Greer, A. Interparticle Delivery and Detection of Volatile Singlet Oxygen at Air/solid Interfaces. *Environ. Sci. Technol.* **2021**, *55*, 3559-3567.

- 17. Jeyapalan, V.; Varadharajan, R.; Veerakanellore, G. B.; Ramamurthy, V. Water: An Underappreciated Reaction Medium for Photodimerizations. *J. Photochem. Photobiol.* A 2021, 420, 113492.
- 18. Geng, W.-C.; Zhang, D.; Gong, C.; Li, Z.; Barraza, K. M.; Beauchamp, J. L.; Guo, D.-S.; Zhang, X. Host–Guest Complexation of Amphiphilic Molecules at the Air–Water Interface Prevents Oxidation by Hydroxyl Radicals and Singlet Oxygen. *Angew. Chemie Int. Ed.* 2020, 59, 12684-12688.
- 19. Mu, C.; Wang, J.; Barraza, K. M.; Zhang, X.; Beauchamp, J. L. Mass Spectrometric Study of Acoustically Levitated Droplets Illuminates Molecular-Level Mechanism of Photodynamic Therapy for Cancer Involving Lipid Oxidation. *Angew. Chemie Int. Ed.* 2019, 58, 8082-8086.
- 20. Zhang, X.; Barraza, K. M.; Upton, K. T.; Beauchamp, J. L. Subtle Changes in Lipid Environment Have Profound Effects on Membrane Oxidation Chemistry. *J. Am. Chem. Soc.* 2018, 140, 17492-17498.
- 21. Zhang, X.; Barraza, K. M.; Beauchamp, J. L. Cholesterol Provides Nonsacrificial Protection of Membrane Lipids from Chemical Damage at Air–Water Interface. *Proc. Natl. Acad. Sci.* 2018, 115, 3255-3260.
- 22. Huang, Y.; Barraza, K. M.; Kenseth, C. M.; Zhao, R.; Wang, C.; Beauchamp, J. L.; Seinfeld, J. H. Probing the OH Oxidation of Pinonic Acid at the Air–Water Interface Using Field-Induced Droplet Ionization Mass Spectrometry (FIDI-MS). J. Phys. Chem. A 2018, 122, 6445-6456.
- 23. Anglada, J. M.; Martins-Costa, M. T. C.; Francisco, J. S.; Ruiz-López, M. F. Photoinduced Oxidation Reactions at the Air–Water Interface. *J. Am. Chem. Soc.* **2020**, *142*, 16140-16155.

- 24. Martins-Costa, M. T. C.; Anglada, J. M.; Francisco, J. S.; Ruiz-López, M. F. Photochemistry of SO₂ at the Air–Water Interface: A Source of OH and HOSO Radicals. *J. Am. Chem. Soc.* 2018, 140, 12341-12344.
- 25. Zhang, D.; Gong, C.; Wang, J.; Mu, C.; Wang, W.; Zhang, X. Beyond Lipid Peroxidation: Distinct Mechanisms Observed for POPC and POPG Oxidation Initiated by UV-Enhanced Fenton Reactions at the Air–Water Interface. J. Mass Spectrom. 2020, 56, e4626.
- 26. Eugene, A. J.; Guzman, M. I. Production of Singlet Oxygen (¹O₂) during the Photochemistry of Aqueous Pyruvic Acid: The Effects of pH and Photon Flux under Steady-State O_{2(aq)} Concentration. *Environ. Sci. Technol.* **2019**, *53*, 12425-12432.
- 27. Pillar, E. A.; Guzman, M. I. Oxidation of Substituted Catechols at the Air–Water Interface: Production of Carboxylic Acids, Quinones, and Polyphenols. *Environ. Sci. Technol.* 2017, 51, 4951-4959.
- 28. Anglada, J. M.; Martins-Costa, M.; Ruiz-López, M. F.; Francisco, J. S. Spectroscopic Signatures of Ozone at the Air–Water Interface and Photochemistry Implications. *Proc. Natl. Acad. Sci.* 2014, 111, 11618-11623.
- 29. Poon, T. H. W.; Pringle, K.; Foote, C. S. Reaction of Cyclooctenes with Singlet Oxygen. Trapping of a Perepoxide Intermediate. *J. Am. Chem. Soc.* **1995**, *117*, 7611-7618.
- 30. Leach, A. G.; Houk, K. N.; Foote, C. S. Theoretical Prediction of a Perepoxide Intermediate for the Reaction of Singlet Oxygen with *trans*-Cyclooctene Contrasts with the Two-Step No-Intermediate Ene Reaction for Acyclic Alkenes. *J. Org. Chem.* **2008**, *73*, 8511-8519.
- 31. Turque, O.; Greer, A.; Wauchope, O. R. Synthetic Feasibility of Oxygen-Driven Photoisomerizations of Alkenes and Polyenes. *Org. Biomol. Chem.* **2020**, *18*, 9181-9190.

- 32. Kwon, B.-M.; Foote, C. S.; Khan, S. I. Chemistry of Singlet Oxygen. 52. Reaction with *trans*-Stilbene. *J. Org. Chem.* **1989**, *54*, 3378-3382.
- 33. Shimizu, N.; Bartlett, P. D. Photooxidation of Olefins Sensitized by α-Diketones and by Benzophenone. A Practical Epoxidation Method with Biacetyl. *J. Am. Chem. Soc.* **1976**, *98*, 4193-4200.
- 34. Maranzana, A.; Ghigo, G.; Tonachini, G. Mechanistic Significance of Perepoxide Trapping Experiments, with Epoxide Detection, in ¹Δ_g Dioxygen Reactions with Alkenes. *J. Org. Chem.* 2003, 68, 3125-3129.
- 35. Malek, B.; Fang, W.; Abramova, I.; Walalawela, N.; Ghogare, A. A.; Greer, A. 'Ene' Reactions of Singlet Oxygen at the Air-Water Interface. *J. Org. Chem.* **2016**, *81*, 6395-6401.
- 36. Fang, Y.; Liu, F.; Bennett, A.; Ara, S.; Liu, J. Experimental and Trajectory Study on the Reaction of Protonated Methionine with Electronically Excited Singlet Molecular Oxygen (a¹Δg): Reaction Dynamics and Collision Energy Effects. J. Phys. Chem. B 2011, 115, 2671-2682.
- 37. Liu, F.; Lu, W.; Yin, X.; Liu, J. Mechanistic and Kinetic Study of Singlet O₂ Oxidation of Methionine by On-Line Electrospray Ionization Mass Spectrometry. *J. Am. Soc. Mass Spectrom.* **2016**, *27*, 59-72.
- 38. Lafferty, W. J.; Solodov, A. M.; Lugez, C. L.; Fraser, G. T. Rotational Line Strengths and Self-Presure-Broadening Coefficients for the 1.27- μ m, $a^1\Delta_g \rightarrow X_3\Sigma g^-$, $\nu = 0$ –0 band of O₂. *Appl. Opt.* **1998**, *37*, 2264-2270.
- 39. Skovsen, E.; Snyder, J. W.; Lambert, J. D. C.; Ogilby, P. R. Lifetime and Diffusion of Singlet Oxygen in a Cell. *J. Phys. Chem. B* **2005**, *109*, 8570-8573.

- 40. Zamadar, M.; Aebisher, D.; Greer, A. Singlet Oxygen Delivery Through the Porous Cap of a Hollow-Core Fiber Optic Device. *J. Phys. Chem. B* **2009**, *113*, 15803-15806.
- 41. Lindig, B. A.; Rodgers, M. A. J.; Schaap, A. P. Determination of the Lifetime of Singlet Oxygen in Water-D₂ Using 9,10-Anthracenedipropionic Acid, a Water-Soluble Probe. *J. Am. Chem. Soc.* **1980**, *102*, 5590-5593.
- 42. Alecu, I. M.; Zheng, J.; Zhao, Y.; Truhlar, D. G. Computational Thermochemistry: Scale Factor Databases and Scale Factors for Vibrational Frequencies Obtained from Electronic Model Chemistries. *J. Chem. Theory Comput.* **2010**, *6*, 2872-2887.
- 43. Marenich, A. V.; Cramer, C. J.; Truhlar, D. G. Universal Solvation Model Based on Solute Electron Density and on a Continuum Model of the Solvent Defined by the Bulk Dielectric Constant and Atomic Surface Tensions. *J. Phys. Chem. B* **2009**, *113*, 6378–6396.
- 44. Maranzana, A.; Ghigo, G.; Tonachini, G. Diradical and Peroxirane Pathways in the $[\pi_2 + \pi_2]$ Cycloaddition Reactions of ${}^{1}\Delta_{g}$ Dioxygen with Ethene, Methyl Vinyl Ether, and Butadiene: A Density Functional and Multireference Perturbation Theory Study. *J. Am. Chem. Soc.* **2000**, 122, 1414-1423.
- 45. Benny, J.; Saito, T.; Moe, M. M.; Liu, J. Singlet O₂ Reactions with Radical Cations of 8-Bromoguanine and 8-Bromoguanosine: Guided-Ion Beam Mass Spectrometric Measurements and Theoretical Treatments. *J. Phys. Chem. A* **2022**, *126*, 68-79.
- 46. Lee, T. J.; Taylor, P. R. A Diagnostic for Determining the Quality of Single-Reference Electron Correlation Methods. *Int. J. Quantum Chem., Quantum Chem. Symp.* **1989**, *36*, 199-207.
- 47. Liakos, D. G.; Sparta, M.; Kesharwani, M. K.; Martin, J. M. L.; Neese, F. Exploring the Accuracy Limits of Local Pair Natural Orbital Coupled-Cluster Theory. *J. Chem. Theory Comput.* **2015**, *11*, 1525-1539.

- 48. Frisch, M. J.; Trucks, G. W.; Schlegel, H. B.; Scuseria, G. E.; Robb, M. A.; Cheeseman, J. R.; Scalmani, G.; Barone, V.; Mennucci, B.; Petersson, G. A. et al. Gaussian 09, Rev. D.01, Gaussian, Inc, Wallingford, CT, 2013.
- 49. Neese, F. Software Update: The ORCA Program System, Version 4.0. *WIREs Comput. Mol. Sci.* **2018**, *8*, e1327.
- 50. Choudhury, R.; Greer, A. Synergism between Airborne Singlet Oxygen and a Trisubstituted Olefin Sulfonate for the Inactivation of Bacteria. *Langmuir* **2014**, *30*, 3599-3605.
- 51. Jabeen, S.; Farag, M.; Malek, B.; Choudhury, R.; Greer, A. A Singlet Oxygen Priming Mechanism: Disentangling of Photooxidative and Downstream Dark Effects. *J. Org. Chem.* 2020, 85, 12505-12513.
- 52. Bartusik, D.; Aebisher, D.; Lyons, A. M.; Greer, A. Bacterial Inactivation by a Singlet Oxygen Bubbler: Identifying Factors Controlling the Toxicity of ¹O₂ Bubbles. *Environ. Sci. Technol.* **2012**, *46*, 12098-12104.
- 53. Manring, L. E.; Foote, C. S. Chemistry of Singlet Oxygen. 44. Mechanism of Photooxidation of 2,5-Dimethylhexa-2,4-Diene and 2-Methyl-2-Pentene. *J. Am. Chem. Soc.* **1983**, *105*, 4710-4717.
- 54. Wilkinson, F.; Helman, W. P.; Ross, A. B. Quantum Yields for the Photosensitized Formation of the Lowest Electronically Excited Singlet State of Molecular Oxygen in Solution. *J. Phys. Chem. Ref. Data* **1995**, *24*, 663-1021.
- 55. Poon, T.; Sivaguru, J.; Franz, R.; Jockusch, S.; Martinez, C.; Washington, I.; Adam, W.; Inoue, Y.; Turro, N. J. Temperature and Solvent Control of the Stereoselectivity in the Reactions of Singlet Oxygen with Oxazolidinone-Substituted Enecarbamates. J. Am. Chem. Soc. 2004, 126, 10498-10499.

- 56. Schweitzer, C.; Schmidt, R. Physical Mechanisms of Generation and Deactivation of Singlet Oxygen. *Chem. Rev.* **2003**, *103*, 1685-1758.
- 57. Alabugin, I. V.; Gomes, G. D. P.; Abdo, M. A. Hyperconjugation. *Wires Comput. Mol. Sci.* **2019**, e1389.
- 58. Donaldson, D. J.; Valsaraj, K. T. Adsorption and Reaction of Trace Gas-Phase Organic Compounds on Atmospheric Water Film Surfaces: A Critical Review. *Environ. Sci. Technol.* 2010, 44, 865-873.
- 59. Sivaguru, J.; Solomon, M. R.; Poon, T.; Jockusch, S.; Bosio, S. G.; Adam, W.; Turro, N. J. The Reaction of Singlet Oxygen with Enecarbamates: A Mechanistic Playground for Investigating Chemoselectivity, Stereoselectivity, and Vibratioselectivity of Photooxidations. *Acc. Chem. Res.* 2008, 41, 387-400.
- 60. Sivaguru, J.; Solomon, M. R.; Saito, H.; Poon, T.; Jockusch, S.; Adam, W.; Inoue, Y.; Turro, N. J. Conformationally Controlled (Entropy Effects), Stereoselective Vibrational Quenching of Singlet Oxygen in the Oxidative Cleavage of Oxazolidinone-Functionalized Enecarbamates through Solvent and Temperature Variations. *Tetrahedron* 2006, 62, 6707-6717.
- 61. Ghogare, A. A.; Greer, A. Using Singlet Oxygen to Synthesize Natural Products and Drugs. *Chem. Rev.* **2016**, *116*, 9994-10034.
- 62. Rana, M. S.; Guzman, M. I. Oxidation of Phenolic Aldehydes by Ozone and Hydroxyl Radicals at the Air–Water Interface. *J. Phys. Chem. A* **2020**, *124*, 8822-8833.
- 63. Hayeck, N.; Mussa, I.; Perrier, S.; George, C. Production of Peroxy Radicals from the Photochemical Reaction of Fatty Acids at the Air–Water Interface. *ACS Earth Sp. Chem.* **2020**, *4*, 1247-1253.

- 64. Anglada, J. M.; Martins-Costa, M.; Francisco, J. S.; Ruiz-López, M. F. Interconnection of Reactive Oxygen Species Chemistry across the Interfaces of Atmospheric, Environmental, and Biological Processes. *Acc. Chem. Res.* **2015**, *48*, 575-583.
- 65. Enami, S.; Hoffmann, M. R.; Colussi, A. J. In Situ Mass Spectrometric Detection of Interfacial Intermediates in the Oxidation of RCOOH_(aq) by Gas-Phase OH-Radicals. *J. Phys. Chem. A* **2014**, *118*, 4130-4137.
- 66. Martins-Costa, M. T. C.; Anglada, J. M.; Francisco, J. S.; Ruiz-Lopez, M. F. Reactivity of Atmospherically Relevant Small Radicals at the Air–Water Interface. *Angew. Chemie Int. Ed.* 2012, *51*, 5413-5417.
- 67. Thompson, K. C.; Rennie, A. R.; King, M. D.; Hardman, S. J. O.; Lucas, C. O. M.; Pfrang, C.; Hughes, B. R.; Hughes, A. V. Reaction of a Phospholipid Monolayer with Gas-Phase Ozone at the Air–Water Interface: Measurement of Surface Excess and Surface Pressure in Real Time. *Langmuir* **2010**, *26*, 17295-17303.

Table of Contents Graphic

